How Magnetic Activity Alters What We Learn from Stellar Spectra

Lorenzo Spina[1,2] , Thomas Nordlander[2,3], Andrew R. Casey[1,2] , Megan Bedell[4] , Valentina D'Orazi[5] , Jorge Meléndez[6] ,
Amanda I. Karakas[1,2] , Silvano Desidera[5], Martina Baratella[5,7], Jhon J. Yana Galarza[6], and Giada Casali[1,8,9]

[1] School of Physics and Astronomy, Monash University, VIC 3800, Australia; lorenzo.spina@monash.edu
[2] ARC Centre of Excellence for All Sky Astrophysics in 3 Dimensions (ASTRO-3D)
[3] Research School of Astronomy and Astrophysics, The Australian National University, Canberra, ACT 2611, Australia
[4] Flatiron Institute, Simons Foundation, 162 Fifth Avenue, New York, NY 10010, USA
[5] INAF—Astronomical Observatory of Padua, Vicolo dell'Osservatorio 5, 35122, Padova, Italy
[6] Universidade de São Paulo, IAG, Departamento de Astronomia, Rua do Matão 1226, São Paulo, 05509-900 SP, Brasil
[7] Department of Physics and Astronomy Galileo Galilei, University of Padua, Vicolo dell'Osservatorio 3, 35122, Padova, Italy
[8] INAF—Arcetri Astrophysical Observatory, Largo E. Fermi 5, 50125 Firenze, Italy
[9] Department of Physics and Astronomy, University of Florence, via G. Sansone 1, 50019 Sesto Fiorentino (Firenze), Italy

Abstract

Magnetic fields and stellar spots can alter the equivalent widths of absorption lines in stellar spectra, varying during the activity cycle. This also influences the information that we derive through spectroscopic analysis. In this study, we analyze high-resolution spectra of 211 sunlike stars observed at different phases of their activity cycles, in order to investigate how stellar activity affects the spectroscopic determination of stellar parameters and chemical abundances. We observe that the equivalent widths of lines can increase as a function of the activity index log R'_{HK} during the stellar cycle, which also produces an artificial growth of the stellar microturbulence and a decrease in effective temperature and metallicity. This effect is visible for stars with activity indexes log $R'_{HK} \geqslant -5.0$ (i.e., younger than 4–5 Gyr), and it is more significant at higher activity levels. These results have fundamental implications on several topics in astrophysics that are discussed in the paper, including stellar nucleosynthesis, chemical tagging, the study of Galactic chemical evolution, chemically anomalous stars, the structure of the Milky Way disk, stellar formation rates, photoevaporation of circumstellar disks, and planet hunting.

Unified Astronomy Thesaurus concepts: Solar analogs (1941); Exoplanets (498); Stellar magnetic fields (1610); Stellar activity (1580); Spectroscopy (1558); Stellar abundances (1577); Solar atmosphere (1477); Stellar atmospheres (1584); Stellar astronomy (1583); Young stellar objects (1834); Galaxy chemical evolution (580); Chemical enrichment (225)

Supporting material: machine-readable tables

1. Introduction

How does chromospheric activity affect the way we interpret stellar spectra? In recent years, both observational and theoretical studies have addressed this fundamental question in stellar astrophysics. The spectroscopic analysis of the sunlike star HD 45184 performed by Flores et al. (2016) revealed that the Fe II lines at 4924, 5018, and 5169 Å, formed in the upper photosphere, have equivalent widths (EWs) that modulate over the stellar activity cycle. More recently, Yana Galarza et al. (2019) showed that the EWs of iron lines in the spectra of the young (∼400 Myr) solar twin HD 59967 increase as a function of chromospheric activity along the stellar cycle. They also demonstrated that the EW variations occur for quantities that depend on the mean line-center optical depth of formation (τ_λ). The direct consequence of this effect is an increase in atmospheric microturbulence (ξ) inferred from the relation between derived Fe abundances and reduced EW, which is proportional to stellar activity level. This effect also drove an artificial decrease of the stellar metallicity ([Fe/H]) and effective temperature (T_{eff}) as a function of chromospheric activity. No variations were observed for surface gravity (log g).

The results from Flores et al. (2016) and Yana Galarza et al. (2019) confirm and conclusively demonstrate the hypothesis advanced by other observational studies, that elemental abundances in stellar spectra can correlate with stellar activity

(e.g., Morel et al. 2003, 2004; Reddy & Lambert 2017; Baratella et al. 2020).

These observations are also supported by theoretical works showing that the presence of a magnetic field can affect spectral lines, both directly through the Zeeman effect and indirectly, due to the magnetically induced changes on the thermodynamical structure of the atmosphere (e.g., Borrero 2008; Fabbian et al. 2010, 2012; Moore et al. 2015; Shchukina & Trujillo Bueno 2015; Shchukina et al. 2016). Since the strength of the magnetic fields in the stellar atmosphere changes following an activity cycle (Babcock 1959), this could explain the observed EW modulation as a function of the activity level. Additionally, the fraction of the stellar surface covered by cool spots changes during the activity cycle (Schwabe 1844), which may play a role in varying the EWs, especially those from lines with low excitation potentials.

In spite of that, magnetic fields and cool star spots are usually neglected in the analysis of stellar spectra, on the unproven assumption that their effects are of secondary importance compared to other sources of uncertainty. Therefore, studying the effects of magnetic activity on stellar spectra is clearly an important new step forward in the progress of techniques for spectroscopic analysis.

With the present study, we aim at extending the experiment performed on a single star by Yana Galarza et al. (2019) to 211 sunlike stars observed 21,897 times by the high-resolution spectrograph High Accuracy Radial velocity Planet Searcher

Table 1
List of the 21,897 HARPS Exposures Employed in This Study—Full Table Available Online at the CDS

Spectrum ID	Star	Project ID	S/N (pxl^{-1})	Airmass	Exptime (s)	BJD
HARPS.2005-04-20T08:37:39.998	α Cen A	075.D-0800(A)	397	1.40	3	2453480.86322119
HARPS.2005-04-20T09:29:10.270	α Cen A	075.D-0800(A)	258	1.56	3	2453480.89899796
HARPS.2005-04-19T03:21:40.666	α Cen A	075.D-0800(A)	370	1.28	5	2453479.64375465
HARPS.2005-04-23T07:46:50.894	α Cen A	075.D-0800(A)	339	1.31	2	2453483.82803507
HARPS.2005-04-21T03:57:14.304	α Cen A	075.D-0800(A)	385	1.22	4	2453481.66851639
…	…	…	…	…	…	…

(This table is available in its entirety in machine-readable form.)

(HARPS) at different phases along their activity cycles (see Section 2 for a detailed discussion on the spectroscopic analysis). Our final goal is to establish—over a large sample of stars covering a wide range of activity levels—how chromospheric activity can indirectly affect the absorption lines of stellar spectra and the information that we infer from spectroscopic analyses (see Section 3). Our results have fundamental implications for several topics in astrophysics that are discussed in Section 4 and include stellar nucleosynthesis, chemical tagging, the study of Galactic chemical evolution, chemically anomalous stars, the structure of the Milky Way disk, stellar formation rates, photoevaporation of circumstellar disks, and planet hunting. Finally, in Section 5, we summarize the outcomes of this experiment and draw our conclusions.

2. Spectroscopic Analysis

Our experiment is carried out over a sample of stellar spectra collected by the HARPS spectrograph (Mayor et al. 2003) and stored in the ESO Archive. The HARPS spectrograph is installed on the 3.6 m telescope at the ESO La Silla Observatory (Chile) and delivers a resolving power of 115,000 over the 383–690 nm wavelength range. The stars and spectra employed in our analysis are selected through the following criteria.

1. We select the stars observed by HARPS with parameters falling within the following intervals: $T_{\rm eff} \in [5500, 6100]$ K, $\log g \in [4.0, 4.8]$ dex, and [Fe/H] $\in [-0.3, 0.3]$ dex. The stellar parameters are obtained by Casali et al. (2020) through the analysis of the co-added HARPS spectrum of each target using the line-by-line differential technique relative to the solar spectrum. This technique has been developed (e.g., Langer et al. 1998; Gratton et al. 2001; Laws & Gonzalez 2001; Meléndez et al. 2009) to obtain precise differential abundances of similar stars, such as binary stars with similar components (e.g., Desidera et al. 2004; Ramírez et al. 2011; Liu et al. 2014; Biazzo et al. 2015; Teske et al. 2016; Nagar et al. 2020) and solar twin stars (e.g., Ramírez et al. 2009; Bedell et al. 2014; Nissen 2015; Spina et al. 2018a).
2. Stars must have at least 10 HARPS spectra available from the ESO public archive with signal-to-noise ratio (S/N) $\geqslant 100$ pixel^{-1} and acquired at airmass $\leqslant 1.6$.
3. Stars must have an intrinsic variation of chromospheric activity of $\Delta \log R'_{\rm HK} \geqslant 0.015$ dex measured over the HARPS spectra.[10] The $\log R'_{\rm HK}$ values are obtained

Table 2
Line List—Full Table Available Online at the CDS

Wavelength (Å)	Species	$\chi_{\rm exc}$ (eV)	EW$_{\rm Sun}$ (mÅ)
4365.896	Fe I	2.990	51.1
4445.471	Fe I	0.087	40.5
4602.001	Fe I	1.608	71.7
4779.439	Fe I	3.415	40.5
4788.757	Fe I	3.237	65.7
…	…	…	

(This table is available in its entirety in machine-readable form.)

through Equation (6), (7), and (8) in Lorenzo-Oliveira et al. (2018), and the measure on each exposure of the Ca II H&K activity indexes $S_{\rm HK}$ are performed according to the methods of Lovis et al. (2011).

Our final sample includes 211 stars observed by HARPS, 21,897 times in total. In Table 1, we list the ID of each spectrum, the corresponding star, the ESO project ID, the S/N measured on the 65th spectral order, the airmass, exposure time, and the barycentric Julian date (BJD) of the observation. Before the analysis, all spectra are normalized and Doppler-shifted using IRAF's `continuum` and `dopcor` tasks.

For the spectroscopic analysis, we employed a line list consisting of 78 Fe I lines, 17 Fe II lines, and 146 lines of other elements (i.e., C, Na, Mg, Al, Si, S, Ca, Sc, Ti, V, Cr, Mn, Co, Ni, Cu, Zn, Y, Zr, and Ba). The wavelengths, species, and excitation potentials of the atomic transitions employed in our study are reported in Table 2. The last columns of the table list the EWs measured in the solar spectrum by Casali et al. (2020). This line list is based on the list employed in Meléndez et al. (2014), which was assembled specifically for the analysis of solar twin stars by selecting preferentially unsaturated lines with minimal blending in the solar spectrum. Equivalent widths of the atomic transitions listed in Meléndez et al. (2014) are measured with `Stellar diff`.[11] This code allows the user to select one or more spectral windows for the continuum setting devoid of absorption features around each line of interest. We employ the same window settings to calculate continuum levels and fit the lines of interest with Gaussian profiles in all of the exposures and the co-added spectrum of each star. The EW measurements are used by the qoyllur-quipu (q2) code (Ramírez et al. 2014) to determine the stellar parameters and chemical abundances for each exposure

---

[10] The $\log R'_{\rm HK}$ index measures the stellar chromospheric flux emission from the photospheric emission in the cores of the Ca H and K lines (Noyes et al. 1984).

[11] `Stellar diff` is a Python code publicly available at https://github.com/andycasey/stellardiff.

Table 3
Equivalent Widths Measured on Each Spectrum—Full Table Available Online at the CDS

Spectrum ID	Star	$\log R'_{HK}$ (dex)	$\lambda 4365.9$ (mÅ)	err $\lambda 4365.9$ (mÅ)	$\lambda 4445.5$ (mÅ)	err $\lambda 4445.5$ (mÅ)	$\lambda 4602.0$ (mÅ)	err $\lambda 4602.0$ (mÅ)	⋯ ⋯
HARPS.2005-04-20T08:37:39.998	α Cen A	−5.154	59.18	0.17	49.14	0.20	81.03	0.17	⋯
HARPS.2005-04-20T09:29:10.270	α Cen A	−5.160	59.31	0.17	49.29	0.22	80.12	0.17	⋯
HARPS.2005-04-19T03:21:40.666	α Cen A	−5.146	59.20	0.20	48.96	0.22	79.66	0.16	⋯
HARPS.2005-04-23T07:46:50.894	α Cen A	−5.151	59.70	0.20	49.94	0.24	80.57	0.20	⋯
HARPS.2005-04-21T03:57:14.304	α Cen A	−5.148	59.37	0.20	49.09	0.20	80.48	0.17	⋯
⋯	⋯	⋯	⋯	⋯	⋯	⋯	⋯	⋯	⋯

(This table is available in its entirety in machine-readable form.)

Table 4
Atmospheric Parameters Determined for Each Exposure—Full Table Available Online at the CDS

Spectrum ID	Star	$\log R'_{HK}$ (dex)	T_{eff} (K)	err T_{eff} (K)	$\log g$ (dex)	err $\log g$ (dex)	[Fe/H] (dex)	err [Fe/H] (dex)	ξ (km s^{-1})	err ξ (km s^{-1})
HARPS.2005-04-20T08:37:39.998	α Cen A	−5.154	5815	5	4.306	0.012	0.223	0.004	1.11	0.01
HARPS.2005-04-20T09:29:10.270	α Cen A	−5.160	5817	5	4.316	0.013	0.222	0.004	1.11	0.01
HARPS.2005-04-19T03:21:40.666	α Cen A	−5.146	5811	5	4.306	0.011	0.221	0.004	1.10	0.01
HARPS.2005-04-23T07:46:50.894	α Cen A	−5.151	5808	5	4.286	0.012	0.228	0.004	1.08	0.01
HARPS.2005-04-21T03:57:14.304	α Cen A	−5.148	5807	4	4.301	0.010	0.217	0.004	1.11	0.01
⋯	⋯	⋯	⋯	⋯	⋯	⋯	⋯	⋯	⋯	⋯

(This table is available in its entirety in machine-readable form.)

Table 5
Chemical Abundances Determined for Each Exposure—Full Table Available Online at the CDS

Spectrum ID	Star	$\log R'_{HK}$ (dex)	[C I/H] (dex)	err [C I/H] (dex)	[Na I/H] (dex)	err [Na I/H] (dex)	⋯ ⋯
HARPS.2005-04-20T08:37:39.998	α Cen A	−5.154	0.00	0.02	0.008	0.009	⋯
HARPS.2005-04-20T09:29:10.270	α Cen A	−5.160	0.015	0.007	0.02	0.02	⋯
HARPS.2005-04-19T03:21:40.666	α Cen A	−5.146	0.000	0.010	0.007	0.007	⋯
HARPS.2005-04-23T07:46:50.894	α Cen A	−5.151	−0.019	0.010	−0.010	0.010	⋯
HARPS.2005-04-21T03:57:14.304	α Cen A	−5.148	0.06	0.06	−0.002	0.011	⋯
⋯	⋯	⋯	⋯	⋯	⋯	⋯	⋯

Note. The differential abundances reported in this table are relative to the co-added spectrum of the corresponding star.

(This table is available in its entirety in machine-readable form.)

through the line-by-line differential analysis, using the co-added spectrum as a reference. The $\log R'_{HK}$ indexes, EWs, atmospheric parameters, and differential abundances determined for each single exposure from our analysis are listed in Tables 3–5. Note that the differential abundances reported in these tables are not relative to the Sun but relative the co-added spectrum of the corresponding star.

3. Results

In this section, we present our results and discuss how stellar activity affects the spectroscopic determination of atmospheric parameters and chemical abundances.

3.1. Stellar Activity and Equivalent Widths

The study by Yana Galarza et al. (2019) on the solar twin HD 59967 revealed that the EWs of iron lines can vary along the stellar activity cycle for quantities that depend on the mean line-center optical depth τ_λ. Namely, lines with $\log \tau_\lambda \gtrsim -1$ do not

show any significant variation along the cycle, but those that form in the external layers of the photosphere have EW values that change with chromospheric activity along the stellar cycle. This effect is also shown in the top panel of Figure 1 where we plot the EW measurements of the Ba II line 5853Å measured from the HD 59967 spectra at different phases of its activity cycle: at higher activity levels, the EW is clearly higher.

We perform a linear fit of the EWs–$\log R'_{HK}$ relation for this and other atomic lines in the HD 59967 spectra. The resulting slopes are plotted in the middle panel pf Figure 1 as a function of $\langle EW \rangle$, the median EW of the line over all exposures. The $\langle EW \rangle$ value can be used as a proxy of the line optical depth τ_λ, as stronger lines form higher above the optical surface of the stellar atmosphere (Gray 1992). The red squares in the middle panel of Figure 1 and the relative error bars represent the binned-averaged slope values and standard deviations calculated at different $\langle EW \rangle$ intervals, respectively. From the plot, we observe that lines with $\langle EW \rangle \gtrsim 50$ mÅ have slopes that are typically positive, indicating that their EWs increase with the
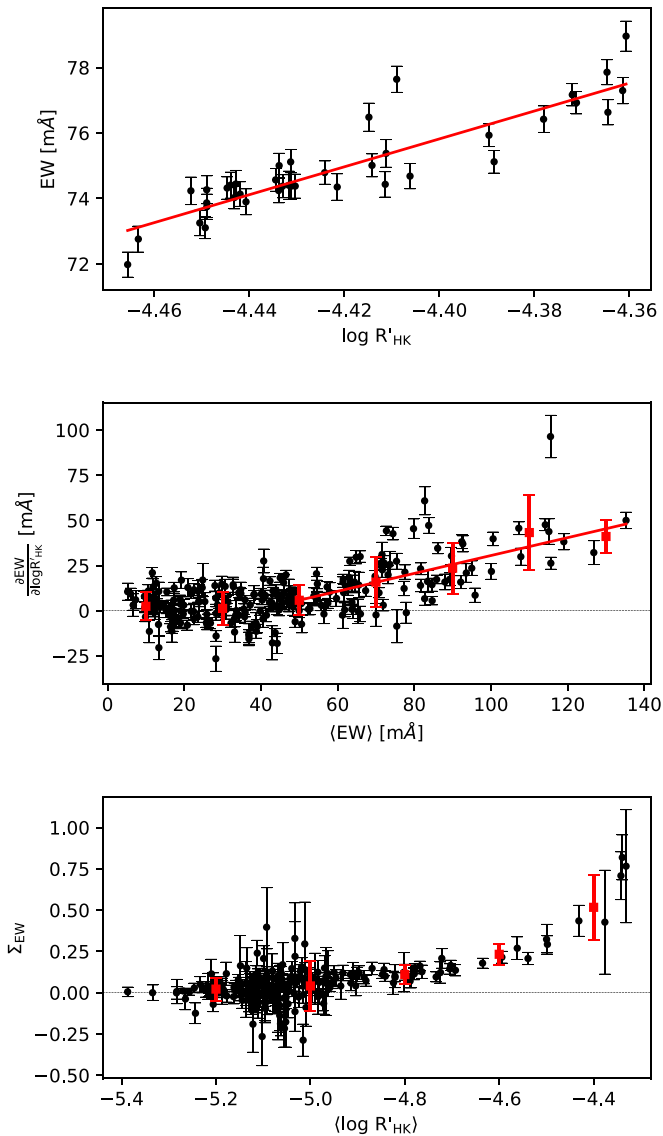
Figure 1. Top panel: equivalent width of the Ba II line at 5853 Å measured from the HARPS spectra acquired for HD 59967 as a function of the stellar log R'_{HK} index. The EW increases as a function of the stellar activity. The red solid line represents the linear fit of the distribution. Middle panel: the black dots are the EW–log R'_{HK} slopes (see top panel) of all of the lines measured in HD 59967 spectra as a function of the median line's EWs (i.e., $\langle EW \rangle$). The averaged values of these slopes at different bins of $\langle EW \rangle$ are plotted as red squares, while their error bars represent the standard deviations within the bin. Lines with $\langle EW \rangle \gtrsim 50$ mÅ have EW–log R'_{HK} slopes that increase with $\langle EW \rangle$. The linear fit of the distribution traced by absorption featured with $\langle EW \rangle > 50$ mÅ is plotted as a red solid line. We refer to its slope value as Σ_{EW}. Bottom panel: the black dots are the Σ_{EW} for all stars in our sample as a function of their median log R'_{HK} index. The red squares and their error bars represent the binned-averaged Σ_{EW} values of the standard deviations at different intervals of $\langle \log R'_{HK} \rangle$.

activity index. All of the other lines have slopes that are typically consistent with zero, meaning that their EWs have not varied significantly during the stellar cycle.

These trends are likely caused by stellar magnetic fields and cool spots affecting the formation of absorption lines observed in stellar spectra. Magnetic fields can affect spectral lines both directly, through the Zeeman effect, and indirectly, due to magnetically induced changes of the temperature and density of the atmospheric plasma in the line formation region. In the

spectrum of a star permeated by magnetic fields of some 10 mT or more, the Zeeman pattern of many absorption lines is considerably wider than the thermal Doppler profile resulting in artificially larger EWs (Babcock 1949). The magnitude of the magnetic intensification of the line depends on the strength of the magnetic field and on the τ_λ of the single line: absorption features that form near the top of the stellar photosphere, where magnetic fields are stronger, undergo a stronger magnetic intensification than lines that form in lower layers. Following the study of Babcock (1949) on the magnetic intensification of stellar absorption lines, many theorists have suggested the presence of magnetic fields to explain the observed phenomenologies of pre-main-sequence stars, such as chemical anomalies or the lithium spread in young clusters (e.g., Uchida & Shibata 1984; Leone & Catanzaro 2004; Leone 2007; Oksala et al. 2018).

On the other hand, the indirect effects of magnetic fields arise from the fact that stellar photospheres become more transparent near magnetic concentrations due to the lower density of the plasma. This allows one to probe into deeper and hotter layers of the stellar atmosphere. The hotter temperatures that the radiation "feels" in these regions weakens the absorption lines with higher potential energy (Fabbian et al. 2012). Since we do not observe weakening of lines as a function of the activity index, we consider that the magnetic intensification predicted by Babcock (1949) is a more likely explanation for the EW modulation than other indirect effects caused by magnetic fields. However, it is also possible that indirect effects due to the presence of strong magnetic fields in the vicinity of stellar spots and plage regions have also affected the absorption lines, creating a certain degree of scatter in the EW measurements, probably further modulated by the rotation of the star.

Finally, the same EW modulation can also be explained by the variation of the stellar surface covered by cold spots along the activity cycle. In fact, cold stellar spots can make the stellar photosphere appear cooler, increasing the EWs of lines with low energy potentials (Gray 1992). Unfortunately, lines with low energy potentials tend to form at smaller τ_λ, which means it is impossible to clearly determine if the main cause of the EW variation is the Zeeman broadening, cool stellar spots, or a combination of the two. It is also possible that the relative importance of the direct and indirect effects of magnetic fields and stellar spots changes as the star ages, due to the drastic variation of spot filling factors, number of faculae, and strength of magnetic fields that stars undergo across the pre-main-sequence and early stages of the main-sequence phases.

Our analysis confirms the conclusions given by Flores et al. (2016) and Yana Galarza et al. (2019) for the solar twins HD 59967 and HD 45184, respectively. However, the goal of this paper is to pass from the analysis of single objects to the study of a larger number of stars of different ages and typical activity levels. To do so, we first perform a linear fit of the relation between the EW–log R'_{HK} slopes and $\langle EW \rangle$ for all of the absorption features with $\langle EW \rangle \geqslant 50$ mÅ. The resulting linear function is presented in the middle panel of Figure 1 as a red solid line. The slope of this linear function is another important parameter that, hereafter, we call Σ_{EW}. Similarly, we calculate Σ_{EW} for all of the other stars in our sample. In the bottom panel of Figure 1, we plot Σ_{EW} values along with their uncertainties as a function of $\langle \log R'_{HK} \rangle$ for all stars in our sample, where $\langle \log R'_{HK} \rangle$ is the median of the activity indexes
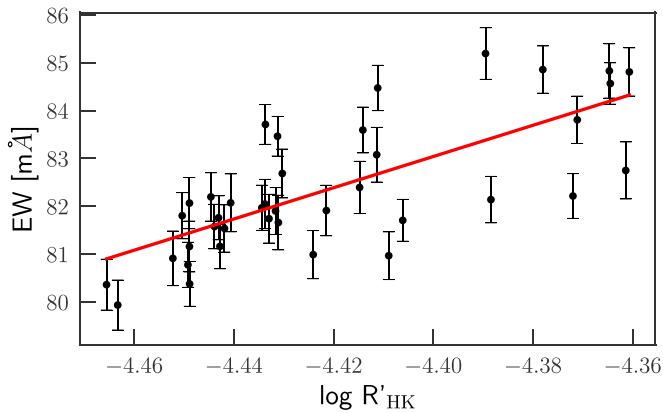
Figure 2. The same as the top panel of Figure 1, but here, Voigt profiles have been used to measure the EWs of the Ba II line instead of Gaussians.

measured at all epochs. The red squares represent the binned-averaged Σ_{EW} values and their standard deviations. The plot shows that the variation of EW during the activity cycle becomes significant for $\langle \log R'_{HK} \rangle \gtrsim -5.0$ dex. Accordingly to the age–log R'_{HK} relation calibrated by Lorenzo-Oliveira et al. (2018) on solar twin stars, stars with $\log R'_{HK} > -5.0$ dex are typically younger than $\sim$5 Gyr. The sensitivity of the EWs to the variation of chromospheric activity during the stellar cycle increases with the median stellar activity, and consequently, it is more significant for younger stars.

Another interesting outcome of this analysis is that the indirect effects of the magnetic fields on stellar spectra are negligible in relation to the Zeeman broadening of atomic lines or the effect of cool stellar spots. This is a general behavior of all of the most active stars in our sample, regardless of other possible key factors, such as the morphology of magnetic fields, that can vary from star to star and that could determine the magnitude by which magnetic fields influence stellar spectra (Moore et al. 2015; Shchukina & Trujillo Bueno 2015).

Finally, we test whether Voigt profiles measure changes in EWs along the stellar cycle that are different than those obtained with Gaussian profiles. In Figure 2, we show the EWs of the Ba II line at 5853 Å measured with Voigt profiles in HD 59967 spectra as a function of log R'_{HK}. These EWs are typically $\sim$8 mÅ larger than those obtained with Gaussians (i.e., see the top panel of Figure 1), because a Voigt profile can better capture the damping wings of stronger lines. However, EW variation as a function of log R'_{HK} traced by a Voigt profile is marginally consistent with that observed using Gaussians: while the first gave an EW–log R'_{HK} slope equal to 33 ± 5 mÅ, the use of Gaussians produced a slope of 43 ± 4 mÅ.

3.2. Stellar Activity and Stellar Parameters

In Section 3.1, we have shown that modulation in chromospheric activity during the stellar cycle can modify the EW of absorption features of a multiplicative factor that depends on $\langle EW \rangle$. Stars with typical log $R'_{HK} > -5.0$ dex are affected by this phenomenon.

As a consequence, the stellar parameters inferred from the simultaneous search for three spectroscopic equilibria of iron lines (i.e., excitation equilibrium, ionization balance, and the relation between log $N_{Fe\,I}$ and the reduced equivalent width EW/λ) can also be indirectly influenced by the stellar chromospheric activity. This is clearly visible in the four

panels of Figure 3. Each panel shows the sensitivity of the four atmospheric parameters (T_{eff}, log g, [Fe/H], and ξ) to the variation in chromospheric activity. For example, $\partial T_{eff} / \partial \log R'_{HK}$ is given as a function of $\langle \log R'_{HK} \rangle$ for all stars in our sample. A negative $\partial T_{eff} / \partial \log R'_{HK}$ means that the T_{eff} value determined though our analysis for a particular star decreases as a function of chromospheric activity during the stellar cycle, while a $\partial T_{eff} / \partial \log R'_{HK}$ consistent with zero indicates that the T_{eff} value has not changed during the stellar cycle.

As shown before, chromospheric activity can induce an increment of lines with typically large EWs. Therefore, higher ξ values are required to balance the relation between abundances and EW/λ. The effect becomes more prominent at larger $\langle \log R'_{HK} \rangle$. This explains why $\partial \xi / \partial \log R'_{HK}$ increases with $\langle \log R'_{HK} \rangle$, as observed in the lower-right panel of Figure 3. An increase of ξ delays the saturation of the curve of growth of each absorption line and, as a consequence, decreases the inferred abundance of the corresponding element (Gray 1992). This effect is clearly visible in the lower-left panel of Figure 3, where δ[Fe/H]/$\delta \log R'_{HK}$ decreases with increasing stellar $\langle \log R'_{HK} \rangle$. The effect described in Section 3.1 also impacts the spectroscopic determination of T_{eff} (see upper-left panel of Figure 3), but it does not significantly affect log g (see upper-right panel of Figure 3).

A detailed inspection of Figure 3 can provide insights on how the chromospheric activity of stars affects our ability to infer T_{eff}, [Fe/H], and ξ from stellar spectra. With this aim, we simultaneously model the $\partial P_i / \partial \log R'_{HK}$–$\langle \log R'_{HK} \rangle$ relations for the ith atmospheric parameters P_i through Markov Chain Monte Carlo (MCMC) simulations. For the procedure, we adopt a model that switches between a null dependence on stellar activity at low log R'_{HK} values to a linear dependence $\partial P_i / \partial \log R'_{HK}$ from stellar activity at high log R'_{HK} values. The model is described as follows:

$$\frac{\partial P_{ij}}{\partial \log R'_{HK}} = \begin{cases} 0 & : x_j < \tau_i \\ a_i \times (x_j - \tau_i) & : x_j \geqslant \tau_i \end{cases} \quad (1)$$

where x_j is the $\langle \log R'_{HK} \rangle$ value of the jth star, and τ_i is the switchpoint of the ith parameter. The model assumes priors for a_i and τ_i that are Normal distributions $\mathcal{N}(\mu, \sigma)$, where μ is the mean, and σ is the standard deviation. Namely, the priors for $a_{T_{eff}}$, $a_{[Fe/H]}$, and a_ξ are $\mathcal{N}(5 \times 10^3, 10 \times 10^3$ K), $\mathcal{N}(0.0, 3$ dex), and $\mathcal{N}(1, 5$ km s^{-1}), respectively. The prior for τ_i is $\mathcal{N}(-5, 1$ dex). We also assume that data points have Gaussian uncertainties of variance $s_{ij}^2 + \zeta_i^2$, where s_{ij} is the uncertainty in $\partial P_i / \partial \log R'_{HK}$ for the jth star, and ζ_i is a parameter that accounts for the possibility that s_{ij} are underestimated and that HARPS observations have not homogeneously sampled the entire stellar cycles. The prior for ζ_i is a half Cauchy function with γ parameters equal to 10 K, 1 dex, and 10 km s^{-1} for T_{eff}, [Fe/H] and ξ, respectively. We ran the simulation with 10,000 samples, half of which are used for burn-in, and we employed the No-U-Turn Sampler (Hoffman & Gelman 2011). The script was written in Python using the pymc3 package (Salvatier et al. 2016).

The convergence of the simulations has been checked by inspecting the traces for each parameter and their autocorrelation plots. The 90% confidence intervals of the posteriors are listed in Table 6: they are well within the ranges allowed by the
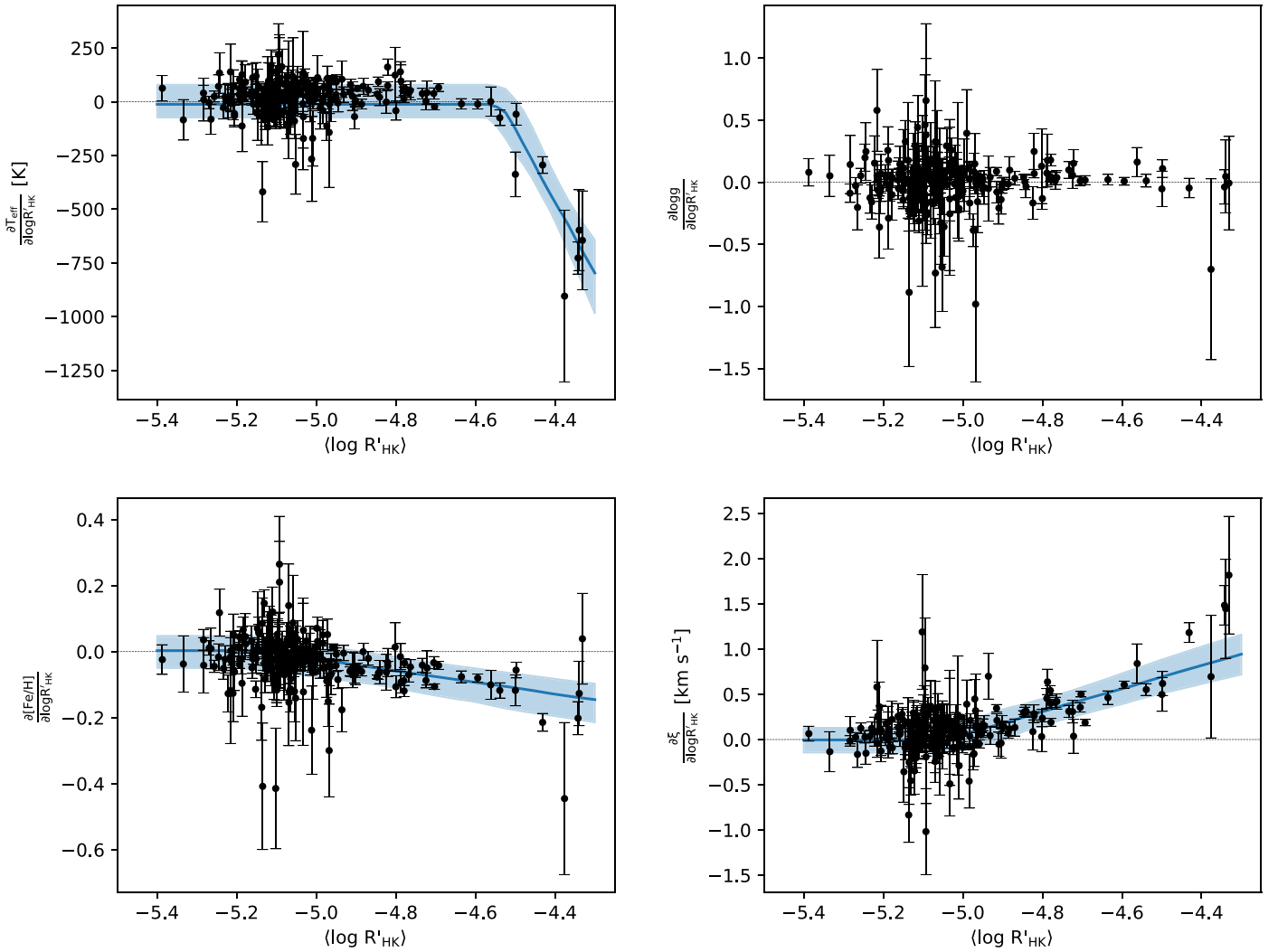
Figure 3. The four panels show the sensitivity of the stellar parameters T_{eff}, log g, [Fe/H], and ξ to the chromospheric activity for all of the stars in our sample as a function of their typical log R'_{HK} indexes. The blue areas and the blue solid lines represent the posterior-probability 90% confidence intervals of the Markov Chain Monte Carlo (MCMC) simulation and the maximum posterior density estimates, respectively.

Table 6
Model Posteriors

Parameter	a [5%, 50%, 95%]	τ [5%, 50%, 95%]	ζ [5%, 50%, 95%]
T_{eff} (K)	−5056, −3510, −2109	−4.58, −4.53, −4.48	40.4, 47.5, 55.0
[Fe/H] (dex)	−0.221, −0.172, −0.123	−5.23, −5.15, −5.07	0.024, 0.029, 0.034
ξ (km s^{-1})	1.02, 1.30, 1.61	−5.10, −5.05, −4.98	0.082, 0.100, 0.118

priors. The 90% confidence intervals of the models resulting from the inference are represented in Figure 3 as the blue areas.

In our model, the spectroscopic determination of the P_i parameter is influenced by activity cycle only if the star has a $\langle \log R'_{HK} \rangle \geqslant \tau_i$. The τ switchpoint inferred for T_{eff} occurs for the highest probability at $\sim$−4.5 dex, which corresponds to solar twins of 1 Gyr (Lorenzo-Oliveira et al. 2018), while the switchpoint inferred for [Fe/H] and ξ happens at $\sim$−5.0, meaning that the determination of these parameters of solar twins younger than 4–5 Gyr is possibly affected by magnetic fields or stellar spots. However, it must be noted that these results are heavily dependent on the master list of absorption features employed in the spectroscopic analysis. In fact, a

reduced use of absorption lines with $\langle EW \rangle \leqslant 50$ mÅ in the spectroscopic analysis would mitigate the impact of magnetic fields or spots on the determination of stellar parameters. However, in this case, it would be more difficult to probe microturbulence due to a lack of strong lines.

Finally, we can predict how a star identical to the Sun (i.e., $T_{eff} = 5770$ K, [Fe/H] = 0.0 dex, and $\xi = 1.0$ km s^{-1}) would look as a function of its chromospheric activity if analyzed with the same line list employed in this study. To do so, we assume that the variation of the ith parameter for the jth star ΔP_{ij} is equal to zero if the stellar activity index is smaller than the switchpoint (i.e., $x_j < \tau_i$), while for larger activity indexes, it is equal to the integral of Equation (1). Our model also includes a
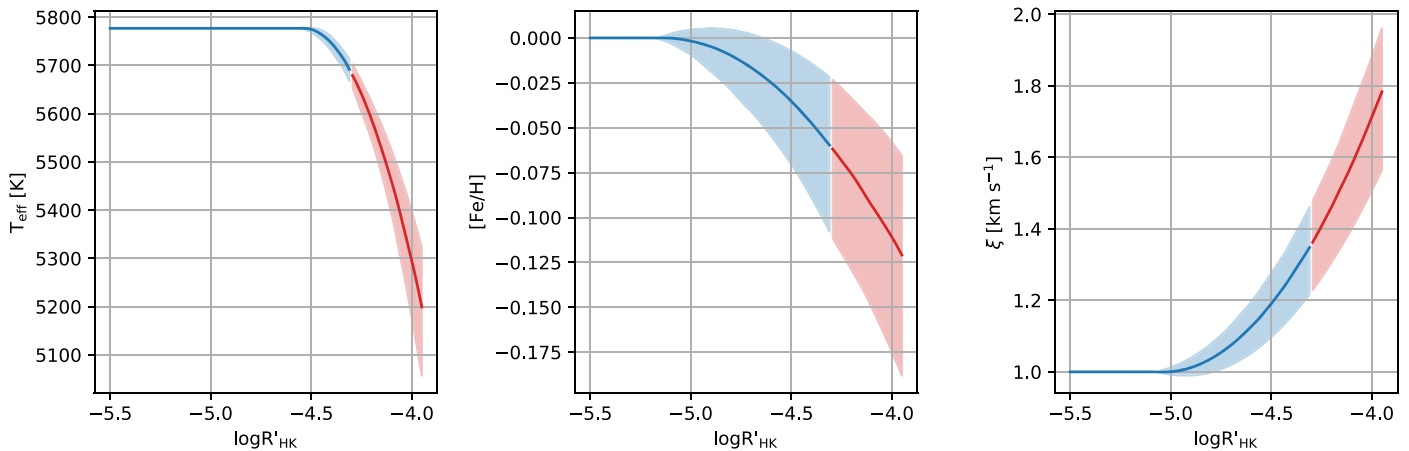
Figure 4. The three panels describe how the stellar parameters $T_{\rm eff}$, [Fe/H], and ξ vary as a function of the stellar activity based on the model described in Equation (2) and the posteriors' distributions obtained through the MCMC simulation. The blue areas represent the 90% confidence intervals within the rage of log $R'_{\rm HK}$ indexes covered by the stars in our sample, while the red areas are the extrapolations of the same model at higher log $R'_{\rm HK}$ values. The solid lines represent the maximum a posteriori estimates. No variation is expected for log g.

second term that depends on ζ_i and that accounts for the possibility that the measured uncertainty $\partial P_i / \partial \log R'_{\rm HK}$ is underestimated. Therefore,

$$\Delta P_{ij} = \begin{cases} 0 & : x_j < \tau_i \\ \dfrac{1}{2}{\rm a}_i \times ({\rm x}_j - \tau_i)^2 + \zeta_i \times ({\rm x}_j - \tau_i) & : x_j \geqslant \tau_i. \end{cases} \quad (2)$$

The ΔP_i probability distribution at each log $R'_{\rm HK}$ has been inferred from the a_i, τ_i, and ζ_i posteriors resulting from the MCMC simulation. In Figure 4, we show the 90% confidence intervals of these distributions. The blue areas highlight the range in log $R'_{\rm HK}$ values covered by our data set, while the red areas are an extrapolation at larger activity indexes of the model fitted to the observations. The maximum variations in the stellar parameters traced by the blue areas are around 100 K, 0.06 dex, and 0.35 km s^{-1} for $T_{\rm eff}$, [Fe/H], and ξ, respectively. These values are similar to the typical uncertainties in atmospheric parameters provided by large spectroscopic surveys observing at optical wavelengths, such as the Gaia-ESO and GALAH surveys (Smiljanic et al. 2014; Buder et al. 2018). However, these surveys targeted pre-main-sequence clusters and stars that are significantly more active than those analyzed here. Thus, even if spectroscopic surveys use different methods of analysis and line lists than those employed in our study, it is possible that the magnetic fields or star spots have affected, to a certain extent, some scientific outcomes of these collaborations (see Section 4 for a discussion on the scientific implications of our result).

Since our data set samples the artificial variation of stellar parameters up to activity indexes of log $R'_{\rm HK} \sim -4.3$ dex, the red areas in Figure 4 represent an extrapolation of this phenomenon at higher indexes, up to log $R'_{\rm HK} \sim -4.0$ dex, values that are typically measured in star-forming regions (Mamajek 2008). Interestingly, ξ values measured for members of these young associations are typically around 2 km s^{-1} (e.g., James et al. 2006; Santos et al. 2008), in agreement with the prediction in Figure 4—right panel. This indicates that magnetic fields and stellar spots play an important role in shaping atomic lines in stellar spectra that are also at the high activity regimes typical of pre-main-sequence stars. Also, the prediction of a $T_{\rm eff}$ variation of ~600 K at log $R'_{\rm HK} \sim -4.0$ dex is partially consistent with the results of other studies that

compared spectroscopic and photometric $T_{\rm eff}$ values for stars in pre-main-sequence stars (Morel et al. 2003; Baratella et al. 2020) finding differences up to 400 K. However, these studies are not able to probe the effect of stellar spots, which have a roughly similar quantitative effect on the temperatures derived from spectroscopic and photometric data (see Fekel et al. 1986; Morel et al. 2003). Thus, the question around the full effect of stellar activity on spectroscopic $T_{\rm eff}$ of T Tauri stars is still open. For instance, it is possible that in extremely active stars (e.g., log $R'_{\rm HK} \sim -4.0$ dex), the Zeeman effect and the consequences of cold stellar spots are counteracted but not fully compensated by the indirect effects that magnetic fields have on the stellar photosphere, which allow stellar spectra to probe into deeper layers where temperatures are higher. This could be possible due to the significantly higher strength of the magnetic fields on T Tauri stars compared to other objects older than a few 10 Myr.

3.3. Stellar Activity and Chemical Abundances

The selective intensification of the strongest absorption lines in stellar spectra affects the determination of chemical abundances in two opposite ways. On one side, the EW intensification produces an increase of chemical abundances. On the other hand, the growth of ξ has the effect of lowering the chemical abundances. Therefore, the net effect on abundances depends on the relative importance of these two reactions to stellar activity, which, in turn, depends on the line list that is used for the analysis.

In Figure 5, we show the dependence of elemental abundances from stellar activity $\partial [X/H]/\partial \log R'_{\rm HK}$ as a function of $\langle \log R'_{\rm HK} \rangle$. While each black dot represents one star of the sample, the red squares and their error bars correspond to the binned-averaged $\partial [X/H]/\partial \log R'_{\rm HK}$ value and its standard deviation at different $\langle \log R'_{\rm HK} \rangle$ intervals. These values are weighted by the $\partial [X/H]/\partial \log R'_{\rm HK}$ uncertainties. The general behavior traced by the red symbols shows that the growth in ξ compensates for the abundance increase for all of the elements. Similarly to what we have observed for [Fe/H] (see Figure 3), the variation of ξ along the cycle of the most active stars is large enough to lower the abundances of Si, Sc, Ti, Mn, Ni, and Cu. This is not surprising; in fact,
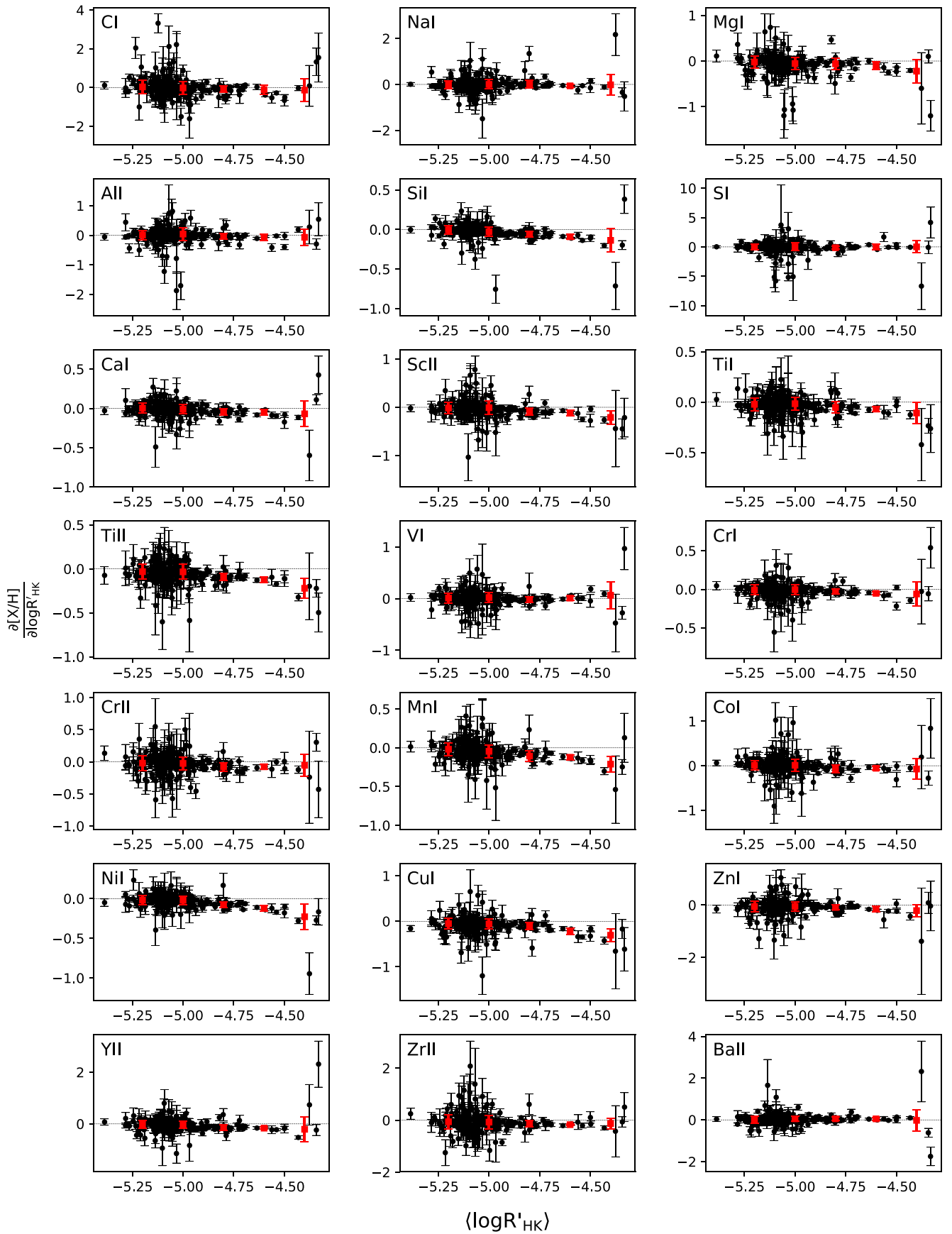
Figure 5. Each panel shows the sensitivity of the X-element abundance to chromospheric activity (i.e., $\partial[X/H]/\partial \log R'_{HK}$) for all stars in our sample as a function of their typical $\log R'_{HK}$ index (black dots). The red squares and their error bars represent the binned-averaged $\partial[X/H]/\partial \log R'_{HK}$ values and standard deviations at different intervals in $\langle \log R'_{HK} \rangle$.

according to our line list, these elements are mostly determined through the measurement of absorption lines that form deep into the stellar photosphere (i.e., $\tau_\lambda > 1$) and that are not significantly intensified by the stellar magnetic fields or cold spots. Furthermore, most of these lines are medium-strong (e.g., EW $\sim$ 40–70 mÅ) and sensitive to ξ. Therefore, for these elements, the increase of line EWs is not enough to compensate for the growth in ξ.

There is a second class of elements formed by C, Na, Al, S, V, Co, Y, and Zr for which the lines used are also formed deep in the atmosphere, but these lines are so weak that they are not sensitive to ξ. Therefore, the change in the abundances of these elements as a function of $\langle \log R'_{HK} \rangle$ is nearly zero.

Finally, we identify a third group of elements (i.e., Mg, Ca, Cr, and Ba) that are detected mostly through strong lines formed in the upper atmosphere. These lines are both sensitive to ξ and intensified by the stellar magnetic fields or cold spots, in a way that one effect counterbalances the other. Therefore, their change in abundances is also nearly zero.

4. Scientific Implications

In the previous section, we have shown how chromospheric activity can affect the stellar parameters and elemental abundances derived from stellar spectra due to the magnetic broadening of the absorption lines and cold stellar spots with $\langle EW \rangle \gtrsim 50$ mÅ. This result provides a definitive explanation to important open questions in the study of the chemical evolution of the Galaxy (e.g., the low metallicity of the local ISM, the metal content of Orion, and the Ba puzzle) as well as key implications for chemical tagging, planet hunting, and many other studies based on stellar parameters determined from spectra of young stars. Below, we discuss the significance of our result to these topics.

4.1. The Anaemia of the Local ISM

The chemical analysis of young ($\lesssim$100 Myr) stars is extremely important in the context of Galactic chemical evolution, as it provides strong constraints to the models of stellar nucleosynthesis. In addition, young stars have not had time to disperse along the Galactic disk; therefore, their chemical content is representative of the ISM's composition at the location where they are observed today. In contrast to models of Galactic chemical evolution (e.g., Minchev et al. 2013; Sanders & Binney 2015; Frankel et al. 2018), independent studies have consistently found that the youngest stars in our Galaxy have a metal content lower than the Sun. For instance, the metal content measured in different star-forming regions located within 500 pc from the Sun (i.e., Chamaeleon, Corona Australis, Lupus, Orion Nebula Cluster, Rho Ophiuchi, and Taurus) is on average equal to [Fe/H] = -0.07 ± 0.03 dex (Cunha et al. 1998; Santos et al. 2008; Biazzo et al. 2011a, 2012; D'Orazi et al. 2011; Spina et al. 2014, 2017), which is $\sim$15% lower than the solar metallicity. Interestingly, members of star-forming regions are found to have ξ values significantly higher than that of the Sun and typically within the range 2.0–2.5 km s^{-1} (e.g., James et al. 2006; Santos et al. 2008; Baratella et al. 2020). The typical $\log R'_{HK}$ index of these stars is $\sim$$-4.0$ dex (Mamajek & Hillenbrand 2008). A comparison of these values to the prediction in Figure 4 suggests that the youngest stars within the solar vicinity appear to be artificially metal poor and have

high ξ as a consequence of their high activity levels (e.g., strong magnetic fields, high coverage of cold stellar spots) that have selectively intensified the strongest atomic lines. According to our predictions, these star-forming regions should actually contain the same amount of metals as the Sun.

4.2. The Metal Content of Orion

The [Fe/H]–$\log R'_{HK}$ prediction in Figure 4 also provides a convincing explanation for the metal content measured in the sub-clusters of the Orion association. Orion is one of the nearest regions ($d \sim$ 350–450 pc) of ongoing star formation where both low- and high-mass stars are formed. It is a complex composed of different sub-clusters with different ages, as the stellar formation burst has spread across the association during the last 20 Myr, triggered by supernovae explosions (Bally 2008). Since SNe II are sites of major nucleosynthesis, these explosions may also chemically enrich parts of the surrounding interstellar gas and, hence, the newly formed next generation of stars (e.g., Reeves 1972; Cunha & Lambert 1992, 1994). Therefore, one would expect that the sequential star formation occurring in Orion should result in a peculiar chemical enrichment with the youngest regions being enhanced in metals relative to older ones. Instead, the Orion Nebula Cluster, which is the youngest region of the Orion association, has been found to be the most metal poor (D'Orazi et al. 2009; Biazzo et al. 2011a, 2011b). Our analysis suggests that a revised analysis of Orion's metal content should be conducted that properly accounts for the effects of the magnetic fields and cold spots on stellar spectra. Providing the first evidence of self-enrichment in a young stellar association would give fundamental insights into stellar nucleosynthesis and, most importantly, on the role that supernovae explosions have in the sequential collapse of molecular clouds, hence, on the origin of stars and stellar clusters.

4.3. The Barium Puzzle

The so-called *barium puzzle* is still one of the most debated open questions around the production of *s*-process elements in the Milky Way. It originated when D'Orazi & Randich (2009) measured [Ba/Fe] ratios in young (<50 Myr) open clusters in the solar vicinity (<500 pc), which showed a $\sim$0.3 dex higher Ba than the value predicted by models of stellar nucleosynthesis (Travaglio et al. 1999; Busso et al. 2001). Further, in contrast to the anomalous Ba overabundance, the abundances of other *s*-process elements such as Y, Zr, La, and Ce relative to Fe were found to be solar (D'Orazi et al. 2012). Interestingly, further studies in young open clusters have shown that additional channels of nucleosynthesis, such as the intermediate neutron-capture process (Cowan & Rose 1977), cannot explain the Ba overabundance compared to other neutron-capture elements (Mishenina et al. 2015).

A new piece of this puzzle was provided by Reddy & Lambert (2015), who analyzed five young (5–200 Myr) local associations and found that they cover an abnormally large range [Ba/Fe] ratios, from +0.07 to +0.32 dex. A further analysis of solar twin stars by Reddy & Lambert (2017) finally provided some clues to the solution of the *Ba puzzle*. Namely, they showed a trend of increasing abundances from the Ba II 5853 Å line with stellar activity among coeval stars. Therefore, they speculated that the high Ba abundance measured in young associations is not nucleosynthetic in origin but associated with

the level of stellar activity. Specifically, they argued that a ξ value derived from Fe lines that form at much larger τ_λ in the photosphere is not sufficient to represent the true broadening imposed by the turbulence of the upper photospheric layers where the Ba II lines form.

Our analysis proceeds in this framework, demonstrating that a relation exists between the EWs of lines formed at small τ_λ into the stellar atmosphere, such as the Ba II lines, and the stellar activity (see Figure 1, top and middle panels). This dependence is visible in our data only for stars with log $R'_{HK} \gtrsim -5.0$ dex (Figure 1, bottom panel).

However, in apparent contradiction to Figure 1, Figure 5 does not show any clear evidence of a systematic positive dependence of Ba abundances from stellar activity. This is not surprising because, as we pointed out in Section 3.3, the increase in ξ as a function of stellar activity has the important consequence of lowering chemical abundances that are derived at high activity levels. Therefore, in our analysis, the increase in ξ is large enough to counterbalance the effect that the Zeeman broadening and stellar spots would have on Ba abundances.

Since the increment in ξ is highly dependent on the line list employed in the analysis and, in particular, on the number of lines with high EW/λ that can trace the turbulence in the upper stellar layers, the use of different line lists can result in a different sensitivities of the ξ parameter to stellar activity. Therefore, a different line list can also produce very different abundances of Ba, whose lines are extremely sensitive to ξ. This explains the large spread in Ba abundances found in young nearby associations by different teams (D'Orazi & Randich 2009; Reddy & Lambert 2015, 2017). For instance, the ξ applied by Reddy & Lambert (2017) for the calculation of Ba abundances was taken from Nissen (2015) and based on a list of weak Fe (EWs $\leqslant 70$ mÅ) formed quite deep in the atmosphere. Therefore, they were using ξ values that do not reflect the extra broadening of absorption lines in the upper layers of active stars, where Ba lines are formed. On the other hand, our line list includes Fe lines with formation depths similar to those of the Ba lines. This explains the apparent contradiction of the large Ba abundances obtained by Reddy & Lambert (2017) with the lack of Ba variation in Figure 5. In a similar way, while our master list contains 78 Fe I lines, the one used by D'Orazi & Randich (2009) was probably too small (only 33 Fe I lines) to adequately probe the turbulence in the upper stellar layers. In fact, while KG-type stars younger than 50 Myr have ξ that are typically greater than 1.5 km s^{-1} (see also D'Orazi et al. 2012), the ξ values estimated in D'Orazi & Randich (2009) are within 0.7 and 1.2 km s^{-1} and very close to their first guess values. In conclusion, the Zeeman effect or stellar spots have intensified the lines used to determined the Ba abundance by D'Orazi & Randich (2009), but in their analysis, this effect was not counteracted by any ξ increase as in our analysis, leaving the Ba abundances anomalously high.

4.4. Chemical Signatures of Planet Engulfment Events

Do stars swallow their own planets? The major consequence of planet engulfment would be a chemical enhancement of the host star due to the pollution of rocky material. If the accreting star has a sufficiently thin convective zone, the planetary material is not too diluted and can produce a significant increase of the atmospheric metallicity, which can be reliably detected (Spina et al. 2015; Church et al. 2020). In fact, such
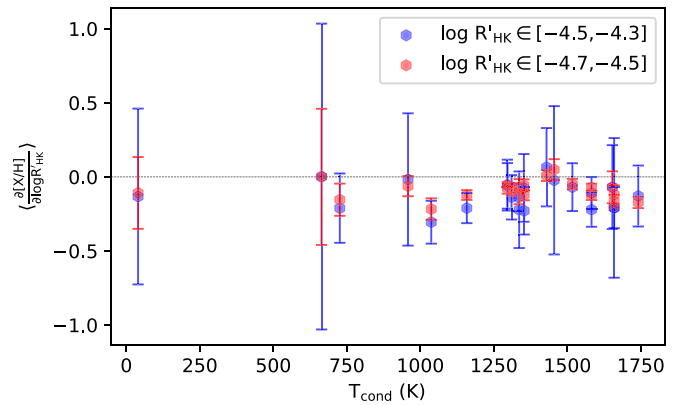
Figure 6. The plot shows the binned-averaged $\partial[X/H]/\partial\log R'_{HK}$ values and standard deviations calculated for the intervals log $R'_{HK} \in [-4.7, -4.5]$ (red) and log $R'_{HK} \in [-4.5, -4.3]$ (blue) as a function of the condensation temperature T_{cond} of the X-element.

dilution will not yield an indiscriminate abundance rise of all of the metals but likely will produce a characteristic chemical pattern that mirrors the composition observed in rocky objects with mostly refractory elements (i.e., those with higher condensation temperatures) being overabundant relatively to volatiles (Chambers 2010).

The chemical signatures of planet engulfment events have been found among members of binary systems (e.g., Ramírez et al. 2015; Teske et al. 2016; Oh et al. 2018; Nagar et al. 2020; Tucci Maia et al. 2019) and open clusters (Spina et al. 2015, 2018b; D'Orazi et al. 2020). Members of the same stellar association are born at the same time and from the same gas; therefore, they should be chemically identical. This indicates that the chemical anomalies found among members of the same association cannot be explained by processes of nucleosynthesis. However, this work poses the suspicion that these chemical anomalies are not actually due to planet engulfment events but instead caused by different activity levels of the members of the same stellar association.

The red and blue symbols in Figure 6 represent the average of the $\partial[X/H]/\partial\log R'_{HK}$ values for stars with log $R'_{HK} \in [-4.7, -4.5]$ and log $R'_{HK} \in [-4.5, -4.3]$, respectively, as a function of the condensation temperature T_{cond} of the X-element listed in Lodders (2003). From this plot, it is evident that some elements are sensitive to the variation in chromospheric activity during the stellar cycle, while others are not. We also observe that there is no clear relation between the sensitivity of an element to the stellar activity and its condensation temperature. Therefore, from these data, there is no evidence in support of the possibility that chromospheric activity could mimic signatures of planet engulfment events in the chemical composition of stars. Instead, there are elements suggesting that the chemical anomalies found so far are genuine and not related to stellar activity. For example, a number of chemically anomalous sunlike stars are older than 5 Gyr (Ramírez et al. 2015; Ramirez et al. 2019; Tucci Maia et al. 2019); therefore, according to our results, their activity levels are not high enough to produce the observed differences in elemental abundances, i.e., $\Delta[Fe/H] \geqslant 0.05$ dex. Furthermore, even when the anomaly has been found among members of young stellar associations, there is no relation between the Fe abundance of the stars and their ξ value (Spina et al. 2015, 2018b; D'Orazi et al. 2020), as one would expect if

the chemical anomaly was driven by an especially high (or low) activity level of the anomalous star compared to the other siblings.

4.5. Chemical Tagging

Similar to a DNA profile, one could use the individual chemical patterns of stars that are not in clusters today to trace them back to a common site of origin (Freeman & Bland-Hawthorn 2002). This approach—commonly called "chemical tagging"—is a powerful tool for Galactic archaeology, which aims at recovering the remnants of the ancient building blocks of the Milky Way (e.g., clusters, super-clusters, and moving groups) that are now dispersed, reconstructing their star formation history and the migration rate of stars within the Milky Way (e.g., Bland-Hawthorn et al. 2010). In fact, the main motivation behind the large-scale spectroscopic surveys of the current decade (e.g., APOGEE, Gaia-ESO, and GALAH; Gilmore et al. 2012; De Silva et al. 2015; Holtzman et al. 2015) has been the acquisition of large and homogeneous sets of spectroscopic data from different environments within the Galaxy to trace its history in space and time.

Regardless of the precision achievable in elemental abundances, the success of chemical tagging relies on the significance of critical factors, including the level of chemical homogeneity within members of open clusters and the chemical diversity between open clusters. Even if it is now established that processes of atomic diffusion (Dotter et al. 2017) and planet engulfment events (Laughlin & Adams 1997) can imprint chemical inhomogeneities among members of the same stellar association, a growing number of studies based on high-precision analysis of solar twin stars are showing that most cluster members on the same evolutionary phase are chemically identical at the typical precision levels reached by large spectroscopic surveys (Liu et al. 2016a, 2016b; Spina et al. 2018a; Nagar et al. 2020).

On the other hand, our analysis shows that magnetic fields or stellar spots can reduce the chemical diversity between stars of different ages, posing a serious challenge for chemical tagging. In fact, while younger stars in our Galaxy should be chemically richer, they also tend to appear poorer in metals than older stars due to the increasing levels of stellar activity (see Figure 4—middle panel). In fact, recent studies have shown how challenging is to reconstruct and reassemble the dissolved stellar associations in the solar vicinity or identify the dispersed family of open clusters solely based on the chemical composition of stars (e.g., Blanco-Cuaresma & Fraix-Burnet 2018; Ness et al. 2018; Casey et al. 2019; Simpson et al. 2019). Therefore, new methods of spectroscopic analysis that could consider the effect of chromospheric activity in the stellar spectra (e.g., Baratella et al. 2020) would pave the way for chemical tagging in the Milky Way disk.

On the other hand, in the context of chemical tagging, it is also possible to use the effect line intensification on stellar spectra to our advantage. In fact, the evidence that equivalent widths of lines can vary during the stellar cycle of quantities that depend on τ_λ allows us to use abundance ratios from lines of the same element formed at different depths in the stellar atmosphere to identify young and active stars in the field or among candidate members of young associations.

4.6. Stellar Ages

It is well known that a star, as it ages, evolves along a determined track in the Hertzsprung-Russell diagram that—to a first approximation—depends on the stellar mass and metallicity. Therefore, if the atmospheric parameters and the absolute magnitude M_V of the star are known with enough precision, it will be possible to determine reasonable estimates of its age and mass (Vandenberg & Bell 1985; Lachaume et al. 1999). In Figure 4, we show that sunlike stars with higher chromospheric activity tend to appear cooler and more metal poor than what they really are. As a consequence, their ages and masses determined though isochrones are systematically overestimated (see also Yana Galarza et al. 2019). This has fundamental implications for all of the studies that aim to trace the nucleosynthetic history of elements in the Galaxy through stellar [X/Fe]–age relations and chemical clocks (e.g., Nissen 2015, 2016; Spina et al. 2016a, 2016b, 2018b; Tucci Maia et al. 2016; Feltzing et al. 2017; Bedell et al. 2018).

4.7. Interstellar Extinction

In recent years, spectroscopic and photometric Galactic surveys have enabled the computation of three-dimensional interstellar extinction maps thanks to accurate stellar atmospheric parameters and line-of-sight distances. This can be achieved by comparing the observed colors to those computed through the stellar parameters and a set of isochrones (e.g., Schultheis et al. 2015; Schlafly et al. 2017). This technique is also extensively used to infer interstellar extinction, which is particularly important for young stars in star-forming regions or pre-main-sequence clusters that are still partially embedded in the parental cloud. In fact, knowledge of the bolometric luminosities of stars in these young associations is vital for a broad variety of topics in stellar astrophysics. These include the studies of mass segregation, dynamical and structural properties of stellar associations before their dissolution, age spread in star-forming regions, rate of star formation in giant molecular clouds and its dependence on time and stellar mass, and the analysis of photoevaporation of circumstellar disks and its impact on planet formation (e.g., Luhman 2008; Sacco et al. 2017; Prisinzano et al. 2019).

Young stars are very active and their spectra are heavily affected by strong magnetic fields. According to our analysis, the $T_{\rm eff}$ of these stars is systematically underestimated due to the effect of chromospheric activity (Figure 4, left panel), which results in an underestimation of the stellar extinction and, hence, to an overestimation of the bolometric luminosity. Therefore, depending on the technique of spectroscopic analysis and the employed line list, stellar activity may have affected the results of observational studies of pre-main-sequence populations.

4.8. Planet Hunting

The possibility of disentangling the effect of stellar activity and jitter from the radial velocity modulation of stars is of paramount importance for spectroscopic surveys that aim at planet detection. This can be achieved through different indicators, such as the bisectors of the spectral cross-correlation function (Queloz et al. 2001), Hα (Bonfils et al. 2007; Robertson et al. 2014), and log $R'_{\rm HK}$ (Noyes et al. 1984; Delisle et al. 2018). More recently, new approaches using these activity indicators and statistical techniques such as Gaussian processes

(e.g., Haywood et al. 2014; Rajpaul et al. 2015; Jones et al. 2017; Delisle et al. 2018) or moving average (e.g., Tuomi et al. 2013) have significantly improved our ability to mitigate the impact of stellar activity on the planetary signal. Recent works have searched for new activity indicators, showing how stellar activity affects spectral lines in different ways (Davis et al. 2017; Thompson et al. 2017; Wise et al. 2018; Zhao & Tinney 2020), which opens up the possibility of using the wealth of information contained in high-resolution spectra to verify the authenticity of a planetary signal (e.g., Dumusque 2018).

Our analysis has shown that not all lines have the same sensitivity to stellar activity but that only the strongest ones (i.e., those with EW > 50 mÅ or with $\log \tau_\lambda < -1$ dex; see also Yana Galarza et al. 2019) vary their EW during the activity cycle (see Figure 1). Therefore, by masking all of the lines for which no variation is expected along the stellar cycle and by detecting all other lines, it is possible to further reduce the noise from stellar activity. This is a very promising possibility that could significantly increase the potential of high-resolution spectrographs in the hunt for planets around sunlike stars. This is especially true for the spectrographs that do not observe the Ca lines, such as Veloce-Rosso (Gilbert et al. 2018) and Minerva-Australis (Addison et al. 2019).

5. Summary

In this study, we analyze 21,897 HARPS spectra of 211 sunlike stars. These stars are observed at high-resolution ($R \sim 115{,}000$) and high S/N ($\geqslant$100 pixel^{-1}) at different phases of their activity cycles. The main goal of this experiment is to provide a quantitative evaluation of the effect that chromospheric activity has on the atmospheric parameters and elemental abundances that we infer from stellar spectra. Our main results can be summarized as follows:

1. The EWs of spectroscopic lines increase with chromospheric activity along the stellar cycle of quantities that depend on the median EW of the line (top panel of Figure 1). Specifically, we observe the largest variation for lines with the highest EW (middle panel of Figure 1).

2. This effect is visible for stars with $\log R'_{\rm HK} > -5.0$ and increases with the activity level of the star (bottom panel of Figure 1). Using the $\log R'_{\rm HK}$–age relation calibrated by Lorenzo-Oliveira et al. (2018) on solar twin stars, we conclude that spectra of sunlike stars younger than 4–5 Gyr are likely affected by this phenomenon.

3. The observed dependence of line EWs from chromospheric activity can be ascribed to the Zeeman broadening of absorption lines that form near the top of the stellar photosphere where magnetic fields are stronger or to the presence of cold stellar spots that can increase the EWs of lines at low energy potentials.

4. Stellar parameters inferred from the simultaneous search for three spectroscopic equilibria of iron lines (i.e., excitation equilibrium, ionization balance, and the relation between $\log N_{\rm Fe\,I}$ and the reduced EWs) are also influenced by the intensification of absorption lines due to stellar activity (Figures 3 and 4). Namely, the EW increase of strong Fe I lines leads to higher ξ values, which, as a consequence, lowers [Fe/H]. This effect is visible for stars with $\log R'_{\rm HK} > -5.0$ (i.e., stars younger than 4–5 Gyr) and increases for more active stars.

We also observe a decrease of $T_{\rm eff}$ with chromospheric activity, which is evident for stars with $\log R'_{\rm HK} > -4.5$ (i.e., younger than 1 Gyr). These effects are not negligible at the typical precision of large spectroscopic surveys. From our analysis, we have not observed any variation in $\log g$.

5. The intensification of absorption line due to chromospheric activity and the consequent rise of ξ have the effect of changing the abundances of specific elements. We have identified three classes of elements. The first class includes the species such as Si, Sc, Ti, Mn, Fe, Ni, and Cu, which are detected mostly through medium-strong lines (EW $\sim$ 40–70 mÅ) and which formed deep in the stellar photosphere ($\tau_\lambda > 1$). These lines are not significantly intensified by magnetic fields or stellar spots, but they are very sensitive to ξ. Therefore, the growth of their EWs is not enough to compensate for the rise of ξ. For this reason, the abundance of these elements decreases as a function of the stellar activity index. The second class of elements includes C, Na, Al, S, V, Co, Y, and Zr. The lines of these elements are very weak and formed deep in the atmosphere. They are not affected by stellar activity, nor sensitive to ξ. Therefore, the change of their abundance is nearly zero. Finally, the elements Mg, Ca, Cr, and Ba are detected through strong lines that formed in the upper atmosphere. These lines are both intensified by stellar activity and sensitive to ξ, in a way that one effect counterbalances the other. Therefore, the change in their abundances is also nearly zero. We stress again that these conclusions depend on the line list that is employed in the spectroscopic analysis.

6. The finding that stellar parameters and abundances can vary as a function of the stellar activity level has several fundamental implications on different topics in astrophysics. For example, studies of Galactic Chemical Evolution will have to consider that the effect described in this paper can artificially affect the chemical abundances obtained through spectroscopic analysis of quantities that depend on the stellar activity, which also scales with the stellar age. On the other hand, the modulation that stellar activity induces on the EWs of the strongest lines (such as the Ba line at 5853 Å, see Figure 1) can be used to trace the phase of the activity cycle in addition to the Mt. Wilson S-index. This can result particularly useful for planet detection techniques.

With this work, we aim at improving the current techniques of spectroscopic analysis by highlighting the limitations and inconsistencies caused by the simplistic assumption that stellar spectra are not affected by magnetic fields and stellar spots. It is central to our progress in different areas of astrophysics that we overcome this difficulty. Therefore, the next step of this research will necessarily be the identification of the main cause(s) of the phenomenon described above (e.g., magnetic fields and/or stellar spots), which will then allow us to find a definitive solution to these limitations (e.g., a new method of spectroscopic analysis and stellar models that incorporate the effects of magnetic fields and stellar spots).

However, the undesired effects of magnetic activity on the spectroscopic analysis can be already hindered by a strategic choice of absorption features in the master list (e.g., see Baratella et al. 2020). From our study, it is clear that the sensitivity of the stellar parameters to the activity index is

mainly due to the use of many medium and strong Fe lines formed in the upper layers of the stellar atmosphere. Namely, out of the 95 Fe I lines in our master list (Table 2), 11 have EWs measured in the solar spectrum that are within 70–80 mÅ, nine fall in the range of 80–90 mÅ, and six have EWs $\geqslant$ 100 mÅ. On the other hand, Yana Galarza et al. (2019) showed that by choosing a list of weaker Fe lines nonsensitive to variations to chromospheric activity they have been able to obtain smaller microturbulences and statistical errors in the spectroscopic analysis of the young solar twin HD 59976. Therefore, a partial solution to the activity problem would be to employ a list of weak Fe lines to determine the stellar parameters, such as the line list used by Nissen (2015), which includes only Fe lines weaker than 70 mÅ. However, an indiscriminate choice of only the weakest Fe lines could also significantly reduce the number of lines at low excitation potential and high reduced EW, necessary to reach the excitation/ionization equilibria. Alternatively, Baratella et al. (2020) proposed a new method based on titanium lines to derive the spectroscopic surface gravity, and most importantly, the microturbulence parameter, while a combination of Ti and Fe lines, is used to obtain effective temperatures.

The use of weak lines can certainly improve the abundance determination of individual elements. However, the problem remains for those element, such as Ba, that are observed only through strong lines formed in the upper layers of the stellar atmosphere. In these cases, the only viable solution could come from magnetohydrodynamical modeling of stellar atmospheres.

Software: qoyllur-quipu (Ramírez et al. 2014), MOOG (Sneden 1973), pymc3 (Salvatier et al. 2016), Stellar diff (https://github.com/andycasey/stellardiff).

ORCID iDs

Lorenzo Spina ⬤ https://orcid.org/0000-0002-9760-6249
Andrew R. Casey ⬤ https://orcid.org/0000-0003-0174-0564
Megan Bedell ⬤ https://orcid.org/0000-0001-9907-7742
Valentina D'Orazi ⬤ https://orcid.org/0000-0002-2662-3762
Jorge Meléndez ⬤ https://orcid.org/0000-0002-4933-2239
Amanda I. Karakas ⬤ https://orcid.org/0000-0002-3625-6951

References

Addison, B., Wright, D. J., Wittenmyer, R. A., et al. 2019, PASP, 131, 115003
Babcock, H. D. 1959, ApJ, 130, 364
Babcock, H. W. 1949, ApJ, 110, 126
Bally, J. 2008, in Handbook of Star Forming Regions, Volume I: The Northern Sky ASP Monograph Publications, ed. B. Reipurth, Vol. 4 (San Francisco, CA: ASP), 459
Baratella, M., D'Orazi, V., Carraro, G., et al. 2020, A&A, 634, A34
Bedell, M., Bean, J. L., Meléndez, J., et al. 2018, ApJ, 865, 68
Bedell, M., Meléndez, J., Bean, J. L., et al. 2014, ApJ, 795, 23
Biazzo, K., Alcalá, J. M., Covino, E., et al. 2012, A&A, 547, A104
Biazzo, K., Gratton, R., Desidera, S., et al. 2015, A&A, 583, A135
Biazzo, K., Randich, S., & Palla, F. 2011a, A&A, 525, A35
Biazzo, K., Randich, S., Palla, F., & Briceño, C. 2011b, A&A, 530, A19
Blanco-Cuaresma, S., & Fraix-Burnet, D. 2018, A&A, 618, A65
Bland-Hawthorn, J., Krumholz, M. R., & Freeman, K. 2010, ApJ, 713, 166
Bonfils, X., Mayor, M., Delfosse, X., et al. 2007, A&A, 474, 293
Borrero, J. M. 2008, ApJ, 673, 470
Buder, S., Asplund, M., Duong, L., et al. 2018, MNRAS, 478, 4513
Busso, M., Marengo, M., Travaglio, C., Corcione, L., & Silvestro, G. 2001, MmSAI, 72, 309
Casali, G., et al. 2020, A&A, submitted
Casey, A. R., Lattanzio, J. C., Aleti, A., et al. 2019, ApJ, 887, 73
Chambers, J. E. 2010, ApJ, 724, 92
Church, R. P., Mustill, A. J., & Liu, F. 2020, MNRAS, 491, 2391
Cowan, J. J., & Rose, W. K. 1977, ApJ, 212, 149
Cunha, K., & Lambert, D. L. 1992, ApJ, 399, 586
Cunha, K., & Lambert, D. L. 1994, ApJ, 426, 170
Cunha, K., Smith, V. V., & Lambert, D. L. 1998, ApJ, 493, 195
Davis, A. B., Cisewski, J., Dumusque, X., Fischer, D. A., & Ford, E. B. 2017, ApJ, 846, 59
De Silva, G. M., Freeman, K. C., Bland-Hawthorn, J., et al. 2015, MNRAS, 449, 2604
Delisle, J. B., Ségransan, D., Dumusque, X., et al. 2018, A&A, 614, A133
Desidera, S., Gratton, R. G., Scuderi, S., et al. 2004, A&A, 420, 683
D'Orazi, V., Biazzo, K., Desidera, S., et al. 2012, MNRAS, 423, 2789
D'Orazi, V., Biazzo, K., & Randich, S. 2011, A&A, 526, A103
D'Orazi, V., Oliva, E., Bragaglia, A., et al. 2020, A&A, 633, 38
D'Orazi, V., & Randich, S. 2009, A&A, 501, 553
D'Orazi, V., Randich, S., Flaccomio, E., et al. 2009, A&A, 501, 973
Dotter, A., Conroy, C., Cargile, P., & Asplund, M. 2017, ApJ, 840, 99
Dumusque, X. 2018, A&A, 620, A47
Fabbian, D., Khomenko, E., Moreno-Insertis, F., & Nordlund, Å. 2010, ApJ, 724, 1536
Fabbian, D., Moreno-Insertis, F., Khomenko, E., & Nordlund, Å. 2012, A&A, 548, A35
Fekel, F. C., Bopp, B. W., Africano, J. L., et al. 1986, AJ, 92, 1150
Feltzing, S., Howes, L. M., McMillan, P. J., & Stonkutė, E. 2017, MNRAS, 465, L109
Flores, M., González, J. F., Jaque Arancibia, M., Buccino, A., & Saffe, C. 2016, A&A, 589, A135
Frankel, N., Rix, H.-W., Ting, Y.-S., Ness, M., & Hogg, D. W. 2018, ApJ, 865, 96
Freeman, K., & Bland-Hawthorn, J. 2002, ARA&A, 40, 487
Gilbert, J., Bergmann, C., Bloxham, G., et al. 2018, Proc. SPIE, 10702, 107020Y
Gilmore, G., Randich, S., Asplund, M., et al. 2012, Msngr, 147, 25
Gratton, R. G., Bonanno, G., Claudi, R. U., et al. 2001, A&A, 377, 123
Gray, D. F. 1992, Sci, 257, 1978
Haywood, R. D., Collier Cameron, A., Queloz, D., et al. 2014, MNRAS, 443, 2517
Hoffman, M. D., & Gelman, A. 2011, arXiv:1111.4246
Holtzman, J. A., Shetrone, M., Johnson, J. A., et al. 2015, AJ, 150, 148
James, D. J., Melo, C., Santos, N. C., & Bouvier, J. 2006, A&A, 446, 971
Jones, D. E., Stenning, D. C., Ford, E. B., et al. 2017, arXiv:1711.01318
Lachaume, R., Dominik, C., Lanz, T., & Habing, H. J. 1999, A&A, 348, 897
Langer, G. E., Fischer, D., Sneden, C., & Bolte, M. 1998, AJ, 115, 685
Laughlin, G., & Adams, F. C. 1997, ApJL, 491, L51
Laws, C., & Gonzalez, G. 2001, ApJ, 553, 405
Leone, F. 2007, ApJL, 667, L175
Leone, F., & Catanzaro, G. 2004, A&A, 425, 271
Liu, F., Asplund, M., Ramirez, I., Yong, D., & Melendez, J. 2014, MNRAS: Lett., 442, L51
Liu, F., Asplund, M., Yong, D., et al. 2016a, MNRAS, 463, 696
Liu, F., Yong, D., Asplund, M., Ramírez, I., & Meléndez, J. 2016b, MNRAS, 457, 3934
Lodders, K. 2003, ApJ, 591, 1220
Lorenzo-Oliveira, D., Freitas, F. C., Meléndez, J., et al. 2018, A&A, 619, A73
Lovis, C., Dumusque, X., Santos, N. C., et al. 2011, ESS, 2, 2.02
Luhman, K. L. 2008, in Handbook of Star Forming Regions, Volume II: The Southern Sky ASP Monograph Publications, ed. B. Reipurth, Vol. 5 (San Francisco, CA: ASP), 169
Mamajek, E. E. 2008, AN, 329, 10
Mamajek, E. E., & Hillenbrand, L. A. 2008, ApJ, 687, 1264
Mayor, M., Pepe, F., Queloz, D., et al. 2003, Msngr, 114, 20
Meléndez, J., Asplund, M., Gustafsson, B., & Yong, D. 2009, ApJL, 704, L66
Meléndez, J., Ramírez, I., Karakas, A. I., et al. 2014, ApJ, 791, 14
Minchev, I., Chiappini, C., & Martig, M. 2013, A&A, 558, A9
Mishenina, T., Pignatari, M., Carraro, G., et al. 2015, MNRAS, 446, 3651

Moore, C. S., Uitenbroek, H., Rempel, M., Criscuoli, S., & Rast, M. P. 2015, ApJ, 799, 150
Morel, T., Micela, G., Favata, F., & Katz, D. 2004, A&A, 426, 1007
Morel, T., Micela, G., Favata, F., Katz, D., & Pillitteri, I. 2003, A&A, 412, 495
Nagar, T., Spina, L., & Karakas, A. I. 2020, ApJ, 888, 9
Ness, M., Rix, H. W., Hogg, D. W., et al. 2018, ApJ, 853, 198
Nissen, P. E. 2015, A&A, 579, A52
Nissen, P. E. 2016, A&A, 593, 65
Noyes, R. W., Hartmann, L. W., Baliunas, S. L., Duncan, D. K., & Vaughan, A. H. 1984, ApJ, 279, 763
Oh, S., Price-Whelan, A. M., Brewer, J. M., et al. 2018, ApJ, 854, 138
Oksala, M. E., Silvester, J., Kochukhov, O., et al. 2018, MNRAS, 473, 3367
Prisinzano, L., Damiani, F., Kalari, V., et al. 2019, A&A, 623, A159
Queloz, D., Henry, G. W., Sivan, J. P., et al. 2001, A&A, 379, 279
Rajpaul, V., Aigrain, S., Osborne, M. A., Reece, S., & Roberts, S. 2015, MNRAS, 452, 2269
Ramirez, I., Khanal, S., Aleo, P., et al. 2015, ApJ, 808, 13
Ramirez, I., Khanal, S., Lichon, S. J., et al. 2019, MNRAS, 490, 2448
Ramírez, I., Meléndez, J., & Asplund, M. 2009, A&A, 508, L17
Ramírez, I., Meléndez, J., & Asplund, M. 2014, A&A, 561, A7
Ramírez, I., Meléndez, J., Cornejo, D., Roederer, I. U., & Fish, J. R. 2011, ApJ, 740, 76
Reddy, A. B. S., & Lambert, D. L. 2015, MNRAS, 454, 1976
Reddy, A. B. S., & Lambert, D. L. 2017, ApJ, 845, 151
Reeves, H. 1972, A&A, 19, 215
Robertson, P., Mahadevan, S., Endl, M., & Roy, A. 2014, Sci, 345, 440
Sacco, G. G., Spina, L., Randich, S., et al. 2017, A&A, 601, 97
Salvatier, J., Wiecki, T. V., & Fonnesbeck, C. 2016, PyMC3: Python Probabilistic Programming Framework, Astrophysics Source Code Library, ascl:1610.016
Sanders, J. L., & Binney, J. 2015, MNRAS, 449, 3479
Santos, N. C., Melo, C., James, D. J., et al. 2008, A&A, 480, 889

Schlafly, E. F., Peek, J. E. G., Finkbeiner, D. P., & Green, G. M. 2017, ApJ, 838, 36
Schultheis, M., Kordopatis, G., Recio-Blanco, A., et al. 2015, A&A, 577, A77
Schwabe, H. 1844, AN, 21, 233
Shchukina, N., Sukhorukov, A., & Trujillo Bueno, J. 2016, A&A, 586, A145
Shchukina, N., & Trujillo Bueno, J. 2015, A&A, 579, A112
Simpson, J. D., Martell, S. L., Da Costa, G., et al. 2019, MNRAS, 482, 5302
Smiljanic, R., Korn, A. J., Bergemann, M., et al. 2014, A&A, 570, A122
Sneden, C. 1973, ApJ, 184, 839
Spina, L., Meléndez, J., Casey, A. R., Karakas, A. I., & Tucci-Maia, M. 2018a, ApJ, 863, 179
Spina, L., Meléndez, J., Karakas, A. I., et al. 2016a, A&A, 593, A125
Spina, L., Meléndez, J., Karakas, A. I., et al. 2018b, MNRAS, 474, 2580
Spina, L., Meléndez, J., & Ramírez, I. 2016b, A&A, 585, A152
Spina, L., Palla, F., Randich, S., et al. 2015, A&A, 582, L6
Spina, L., Randich, S., Magrini, L., et al. 2017, A&A, 601, A70
Spina, L., Randich, S., Palla, F., et al. 2014, A&A, 568, A2
Teske, J. K., Khanal, S., & Ramírez, I. 2016, ApJ, 819, 19
Teske, J. K., Shectman, S. A., Vogt, S. S., et al. 2016, AJ, 152, 167
Thompson, A. P. G., Watson, C. A., de Mooij, E. J. W., & Jess, D. B. 2017, MNRAS, 468, L16
Travaglio, C., Galli, D., Gallino, R., et al. 1999, ApJ, 521, 691
Tucci Maia, M., Meléndez, J., Lorenzo-Oliveira, D., Spina, L., & Jofré, P. 2019, A&A, 628, 126
Tucci Maia, M., Ramírez, I., Meléndez, J., et al. 2016, A&A, 590, A32
Tuomi, M., Anglada-Escudé, G., Gerlach, E., et al. 2013, A&A, 549, A48
Uchida, Y., & Shibata, K. 1984, PASJ, 36, 105
Vandenberg, D. A., & Bell, R. A. 1985, ApJS, 58, 561
Wise, A. W., Dodson-Robinson, S. E., Bevenour, K., & Provini, A. 2018, AJ, 156, 180
Yana Galarza, J., Meléndez, J., Lorenzo-Oliveira, D., et al. 2019, MNRAS, 490, 86
Zhao, J., & Tinney, C. G. 2020, MNRAS, 491, 4131